NJC

ROYAL SOCIETY OF CHEMISTRY

PAPER

View Article Online
View Journal | View Issue

Check for updates

Cite this: *New J. Chem.*, 2026, **50**, 1844

Structural and antimicrobial studies on a tricarbonyl rhenium(I) complex with the 6,7-dimethyl-2-(pyridin-2-yl)quinoxaline ligand

Sibusiso A. Sithole,[a] Ahmed M. Mansour,*[bc] Frederick P. Malan,[d] Gurusamy Manikandan,[e] David R. Katerere,[e] Ola R. Shehab[b] and Amanda-Lee E. Manicum*[a]

Received 20th October 2025,
Accepted 8th December 2025

DOI: 10.1039/d5nj04125b

rsc.li/njc

A new tricarbonyl rhenium(I) complex featuring 6,7-dimethyl-2-(pyridin-2-yl)quinoxaline (**1**) was synthesized and characterized using spectroscopic and crystallographic techniques, supported by density functional theory (DFT) calculations. Ligand **1** acts as a bidentate *N*,*N*′-donor, coordinating through the pyridyl and quinoxaline nitrogen atoms to form a *fac*-[ReCl(CO)$_3$(**1**)] (**2**) complex. Single-crystal X-ray diffraction analysis revealed an octahedral geometry around the Re(I) centre, with the three carbonyl ligands adopting a *facial* arrangement. Hirshfeld surface analysis indicated that weak C–H···Cl interactions play a significant role in crystal packing stabilization. DFT and time-dependent DFT (TDDFT) calculations confirmed the observed experimental geometry and provided insights into the metal–ligand bonding, charge distribution, and electronic transitions. The combined results highlight the structural and electronic features that contribute to the stability and potential bioactivity of this rhenium(I) tricarbonyl complex. The antimicrobial assay indicated that the rhenium metal complex (**2**) was superior to the ligand (**1**) in activity against six different microbial species, but inferior to the standard antimicrobial agents.

Open Access Article. Published on 09 January 2026. Downloaded on 6/12/2026 11:25:46 AM.
This article is licensed under a Creative Commons Attribution-NonCommercial 3.0 Unported Licence.

1. Introduction

Tricarbonyl Re(I) compounds have attracted a lot of attention due to their diverse photophysical and photochemical properties, which make them ideal for a variety of applications, such as biomolecular labelling,[1] light-emitting devices,[2] and the reduction of carbon dioxide.[3] Large Stokes shifts, a long-lived excited state, and high quantum emission efficiency are typical of tricarbonyl rhenium(I) complexes, which reduce the self-quenching effects frequently observed when organic dyes are used to label biomolecules fluorescently. When using time-resolved microscopy to investigate tissue samples, the advantage of a large Stokes shift presents a challenge in filtering out interference from short-lifetime biomolecular autofluorescence from the desired signal.

Rhenium, which is frequently overlooked in medical applications in favour of other metals like iron and ruthenium, has attracted more attention in medicinal chemistry, including as anticancer medicines, radiopharmaceutical imaging agents, and, more recently, antibacterial compounds.[4–7] A search in the literature shows that tricarbonyl compounds of rhenium are particularly appealing because of their extremely low *in vivo* toxicity.[8–10] In addition, this family of metal carbonyls has been studied extensively in the context of photoactivated therapy due to their extensive photophysical characteristics.[11] Because of their favourable intracellular localization and organelle targeting,[12] rhenium(I) complexes have already been proven to be helpful as cellular imaging agents, and they now offer the prospect of combining their activities as fluorescence microscopy imaging agents with *in vivo* radio-imaging.[13] The chemical alteration of the *fac*-[Re(CO)$_3$]$^+$ motif can be utilized to control their lipophilicity and improve their cellular absorption and cytotoxicity.[14,15]

According to a literature search, certain Re(I) tricarbonyl complexes showed promising antimicrobial activity.[4–7,16–19] Carbonyl rhenium compounds have shown activity against Gram-positive bacteria, especially *Staphylococcus aureus*, including both methicillin-sensitive (MSSA) and methicillin-resistant (MRSA)

[a] *Department of Chemistry, Tshwane University of Technology, Pretoria, 0001, South Africa. E-mail: ManicumAE@tut.ac.za*
[b] *Department of Chemistry, Faculty of Science, Cairo University, Gamma Street, Giza, 12613, Egypt. E-mail: mansour@sci.cu.edu.eg, inorganic_am@yahoo.com, mansour_am@uaeu.ac.ae*
[c] *Department of Chemistry, United Arab Emirates University, Al-Ain, United Arab Emirates*
[d] *Department of Chemistry, University of Pretoria, Pretoria, 0001, South Africa*
[e] *Department of Pharmaceutical Sciences, Tshwane University of Technology, Pretoria, 0001, South Africa*

 This journal is © The Royal Society of Chemistry and the Centre National de la Recherche Scientifique 2026

Open Access Article. Published on 09 January 2026. Downloaded on 6/12/2026 11:25:46 AM.
This article is licensed under a Creative Commons Attribution-NonCommercial 3.0 Unported Licence.

strains.[20–22] Certain hetero-trimetallic tricarbonyl rhenium complexes linked to a peptide nucleic acid backbone were identified as innovative antibacterial drugs specifically targeting Gram-positive bacteria, such as *Bacillus subtilis* and *Staphylococcus aureus*.[23] Some cationic tricarbonyl Re(I) complexes of triazole derivatives were more effective against *Staphylococcus aureus* than the neutral one.[24] The mechanism of action of the mixed ligand Re(I) complex functionalized with both 2,2′-bipyridine and the clotrimazole drug against *Staphylococcus aureus* demonstrated the interference with peptidoglycan formation by targeting the cytoplasmic membrane.[25] The significant activity, blood stability, and lack of carbon monoxide leakage served as the driving forces behind this investigation.[25] The bisquinoline tricarbonyl Re(I) complexes demonstrated a dual mode of action against both Gram-positive and Gram-negative bacteria, with the latter requiring exposure to light to be active, as well as moderate cytotoxicity against human embryonic kidney (HEK293) cells.[26] However, the chemical features of tricarbonyl rhenium complexes that make them such promising therapeutic agents are still unknown.

In the present contribution, we synthesized and structurally characterized 6,7-dimethyl-2-(pyridin-2-yl)quinoxaline **1** and its new tricarbonyl rhenium(I) complex **2** (Scheme 1) using different analytical and spectroscopic tools including single crystal X-ray diffraction analysis of both compounds. Due to the variety of biological effects that **1** provides, we have selected it as an auxiliary ligand for **2**.[27–30] The experimental investigation was supported by density functional theory (DFT) calculations to better understand the nature of the observed electronic absorption transitions and investigate the natural charge of the metal ion upon coordination to the quinoxaline ligand, the strength of metal–ligand (M–L) bonds, and the hybridization. Electronic absorption spectra were recorded in a variety of polar (a)protic solvents to investigate the solvatochromic features of **2**. With reference to two standard antimicrobial agents, voriconazole and ciprofloxacin, the free ligand and its rhenium(I) complex were tested for possible antimicrobial activity.

2. Results and discussion

2.1. Synthesis and characterization

As shown in Scheme 1, to prepare 6,7-dimethyl-2-(pyridin-2-yl)-quinoxaline **1**, a mixture of 4,5-dimethyl-benzene-1,2-diamine and one equivalent of 2-acetylpyridine was heated to reflux in methanol for 24 hours under an argon atmosphere.[31] This was performed with a catalytic amount of SiO_2 and diluted hydrochloric acid (10% v/v). Following completion, the mixture was allowed to cool to ambient temperature before being diluted with water and neutralized using an aqueous solution of sodium carbonate. The quinoxaline ligand was structurally characterized by FT-IR spectroscopy (Fig. S1), NMR spectroscopy (^{1}H, Fig. S2; and ^{13}C, Fig. S3) and single crystal X-ray diffraction (*vide infra*). To prepare **2**, ligand **1** was added to the solution of *fac*-$[Re(CO)_3(OH_2)_3]^+$, which was initially prepared by treating the acidified aqueous solution (in HCl) of *fac*-$[NEt_4]_2[ReBr_3(CO)_3]$ with silver nitrate in a 1 : 3 ratio. Next, the reaction mixture was stirred at room temperature for 24 h, upon which a brown precipitate formed, which was recrystallized in a 1 : 3 acetone/water solution, resulting in the formation of red crystals, which were suitable for collection with X-ray diffraction. The tricarbonyl rhenium(I) complex **2** was structurally characterized by FT-IR spectroscopy (Fig. S4), NMR spectroscopy (^{1}H, Fig. S5; and ^{13}C, Fig. S6) and single crystal X-ray diffraction. The symmetrical and anti-symmetrical stretching modes of the three CO molecules arranged in a *facial* pattern are responsible for the two noticeable stretching bands at 2016 and 1881 cm^{-1} in the infrared spectrum of **2** (Fig. S4). The ^{1}H NMR spectrum of **2** (Fig. S5), in $CDCl_3$, consists of three singlet signals at δ_H = 9.58, 8.67 and 8.01 ppm, assigned to quinoxaline protons (H3, H8 and H5), as well as two doublets and two triplets assigned to the pyridine moiety, namely δ_H = 9.23, 8.48, 8.16 and 7.63 ppm (H6, H3, H4 and H5), respectively. The ^{13}C NMR spectrum of **2** (in $CDCl_3$) shows three CO signals at around δ = 197.0, 196.3,

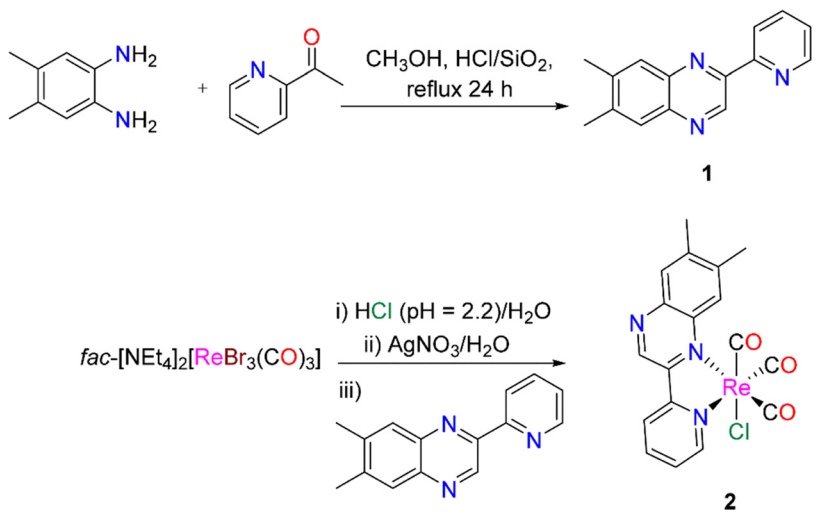

Scheme 1 Synthetic procedures of 6,7-dimethyl-2-(pyridin-2-yl)quinoxaline **1**[31] and its chlorido tricarbonyl Re(I) complex (**2**).

Open Access Article. Published on 09 January 2026. Downloaded on 6/12/2026 11:25:46 AM. This article is licensed under a Creative Commons Attribution-NonCommercial 3.0 Unported Licence.

and 188.2 ppm (Fig. S6). When comparing the ^{1}H NMR spectra of **1** and **2** in the same solvent,[31] quinoxaline-H3 and pyridine-H6 experience substantial de-shielding and migrate downfield due to their role in the formation of **2**. Based on the results of infrared and NMR spectroscopy, the rhenium complex is composed of three CO molecules in a *facial* arrangement, as well as coordination of 6,7-dimethyl-2-(pyridin-2-yl) quinoxaline in a bidentate coordination mode.

2.2. Crystal structures of 1 and 2

The gradual evaporation of **1** in a dichloromethane solution produced suitable single crystals for X-ray crystallographic analysis. Table S1 presents the crystallographic data of **1**, and Fig. 1 shows the molecular structure of **1**. The quinoxaline ligand **1** crystallizes in the orthorhombic space group *Pbca* with a = 11.9662(4) Å, b = 7.4448(3) Å, and c = 26.0051(9) Å. The unit cell of **1** is made up of eight molecules (Fig. S7). The pyridine ring is rotated from the equatorial plane by 24.1° for the N1–C1–C2–C3 dihedral angle (Fig. 1), consistent with weak π–π conjugation between the rings. The absence of classical hydrogen bonds is compensated by an intramolecular C–H···N interaction (2.610 Å), which promotes the formation of one-dimensional chains through blue-shifting hydrogen bonding (Fig. S8).

In other words, the quinoxaline ligand forms an infinite chain structure through the latter-mentioned blue-shifting hydrogen bond interaction. Selected bond lengths of **1** are shown in Table S2 along with their computed equivalents (*vide infra*).

On the other hand, by slowly evaporating **2** in an acetone/water solution, suitable single crystals were obtained for X-ray crystallographic analysis. The crystallographic data are shown in Table S1. The asymmetric unit of **2** is shown in Fig. 2, along with part of its crystal data. Crystallization of **2** occurs in the orthorhombic space group $Pca2_1$ with a = 7.4384(3) Å, b = 15.5722(6) Å, and c = 29.4061(11) Å. The asymmetric unit consists of two crystallographically unique complex molecules, as well as two water molecules of crystallization (Fig. 2). The unit cell of **2** is composed of eight complex molecules and eight water molecules (Fig. S9). The molecular structure of **2** exhibits slightly distorted octahedral geometries of both molecules around the rhenium(I) centres. The Re(I) atom is coordinated by a bidentate *N*,*N*′-donor quinoxaline ligand, three carbonyl groups in a *facial* arrangement, and a terminal chlorido ligand. The Re–N bond distances [in molecule A for Re1A–N1A = 2.171(7) Å, in molecule B for Re1B–N1B = 2.155(7) Å; in molecule A for Re1A–N2A = 2.213(6) Å, in molecule B for Re1B–N2B = 2.225(6) Å] indicate slightly stronger bonding to the pyridine nitrogen than to the quinoxaline nitrogen, consistent with their differing basicity. The Re–C distances in both molecules [1.906(8)–1.935(10) Å] are typical for Re(I) carbonyls, while the Re–Cl bond length in both molecules [2.501(2)–2.502(2) Å] falls within the expected range for *fac*-[$Re(CO)_3Cl(N,N)$] species. It was also noted that the Re bond with quinoxaline's nitrogen is approximately 0.05 Å longer than the one with pyridine's nitrogen.[32,33] Among the Re–C bonds, the *trans*-Re–C bond to quinoxaline's nitrogen is the shortest due to the expected *trans* effect of the coordinated ligands. Given that certain tricarbonyl Re(I) complexes exhibit photosensitivity and that the release of CO from these organometallic compounds occurs sequentially, commencing with the generation of photolabile dicarbonyl species, we hypothesized that the weakly coordinated CO would be released first. In this case, C3A–O3 may be the first to leave the coordination sphere, while C2A–O1 is expected to be the least likely to leave. The molecular packing reveals significant weak C–H···Cl interactions (C···Cl ≈ 3.002 Å and C···Cl ≈ 2.748 Å) linking adjacent molecules into a three-dimensional network (Fig. 3). In addition, strong hydrogen bonds were observed *via* the lattice water molecules within the structure (Fig. S9 in the SI). These blue-shifting hydrogen bonds, together with van der Waals interactions among CO groups and the strong O–H···X (X = N, O, Cl) hydrogen bonds, play a dominant role in stabilizing the crystal lattice. The observed bond parameters are in excellent agreement with those found for structurally related *fac*-[$Re(CO)_3Cl(N,N')$] complexes.

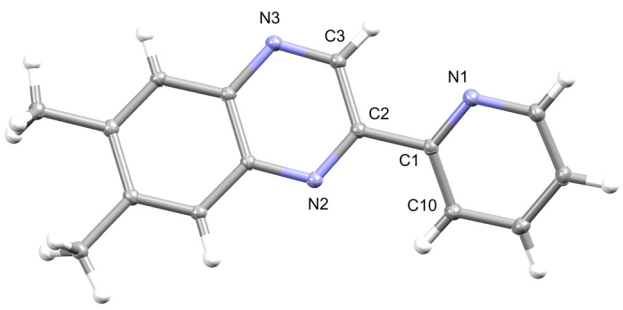

Fig. 1 Molecular structure of **1** (thermal ellipsoids are displayed at the 50% probability level).

2.3. Hirshfeld surface analysis

Using CrystalExplorer 17.5 software,[34] Hirshfeld surface analysis[35] was performed on **1** and **2** to gain additional insight into the intermolecular interactions. As shown in Fig. 4 and 5, on the Hirshfeld surface, interactions separated by the sum of the van der Waals radii are indicated by the white regions observed over the *d*-norm. The red and blue colours, on the other hand, indicate distances that are less than (near contact) or greater than (far contact) the sum of the van der Waals radii. Fig. 4a and 5a show the total two-dimensional fingerprint plots for **1** and **2**, respectively. Fig. 4b–d and 5b–d illustrate the other interactions in the studied compounds, including O···H/H···O, N···H/H···N, and Cl···H/H···Cl, along with their respective contributions to the Hirshfeld surface. As illustrated in Fig. 4b, the most notable interactions in **1**, aside from C–H, are H···N/N···H (15.4%), as previously demonstrated in the crystal structure part. On the other hand, it is evident that H···Cl/Cl···H and H···O/O···H have a major influence on the stabilization of the crystal structure of **2** and molecular packing, while the H···N/N···H interaction has a smaller effect, with a relative contribution of 6.8%. Given that they make up 17.4% of the

 This journal is © The Royal Society of Chemistry and the Centre National de la Recherche Scientifique 2026

Open Access Article. Published on 09 January 2026. Downloaded on 6/12/2026 11:25:46 AM.
This article is licensed under a Creative Commons Attribution-NonCommercial 3.0 Unported Licence.

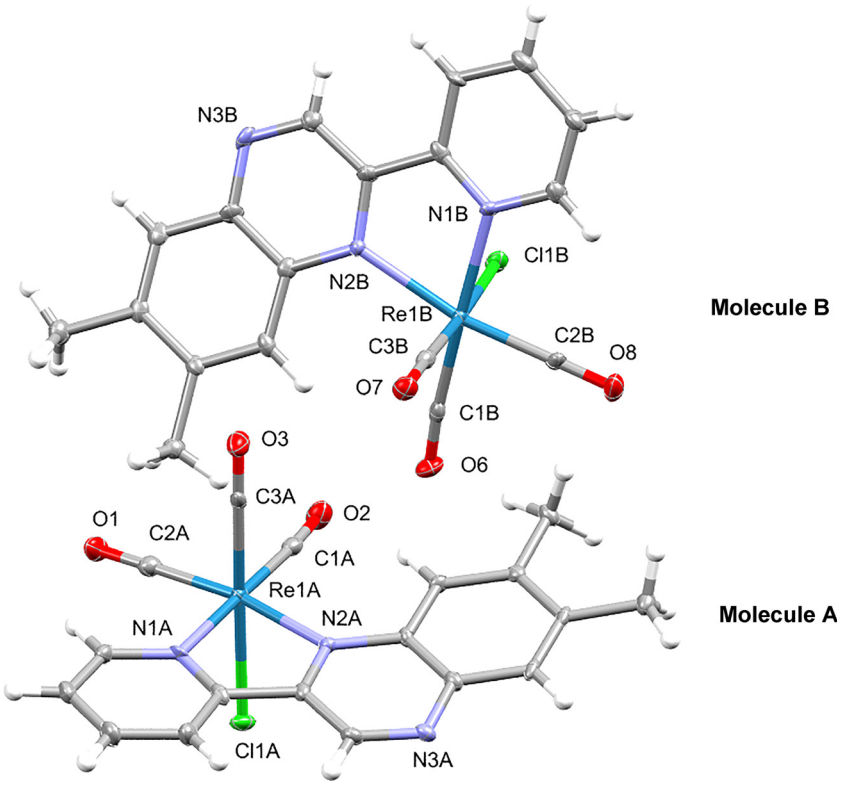

Fig. 2 Molecular structure of **2** (thermal ellipsoids are displayed at the 50% probability level). Two molecules of water are omitted for clarity. Bond lengths in (Å): Re1A–C1A 1.934(9), Re1A–C2A 1.916(8), Re1A–C3A 1.935(10), Re1A–N1A 2.171(7), Re1A–N2A 2.213(6), Re1A–Cl1A 2.501(2), C1A–O2 1.135(11), C2A–O1 1.139(10), C3A–O3 1.130(12), Re1B–C1B 1.931(9), Re1B–C2B 1.906(8), Re1B–C3B 1.907(9), Re1B–N1B 2.155(7), Re1B–N2B 2.225(6), Re1B–Cl1B 2.502(2), C1B–O6 1.125(11), C2B–O8 1.146(10), C3B–O7 1.159(11). Bond angles (°): C1A–Re1A–Cl1A 93.7(2), C1A–Re1A–C2A 85.0(3), C1A–Re1A–C3A 88.1(4), C1A–Re1A–N1A 178.5(3), C1A–Re1A–N2A 105.6(3), Cl1A–Re1A–C3A 177.2(3), Cl1A–Re1A–C2A 93.0(3), Cl1A–Re1A–N1A 84.81(19), Cl1A–Re1A–N2A 83.43(16), C3A–Re1A–C2A 89.2(3), C3A–Re1A–N1A 93.3(3), C3A–Re1A–N2A 94.1(3), C2A–Re1A–N1A 94.6(3), C2A–Re1A–N2A 169.0(3), N1A–Re1A–N2A 74.7(3), C1B–Re1B–Cl1B 89.5(2), C1B–Re1B–C2B 85.6(3), C1B–Re1B–C3B 90.1(4), C1B–Re1B–N1B 173.3(3), C1B–Re1B–N2B 105.0(3), Cl1B–Re1B–C3B 176.6(2), Cl1B–Re1B–C2B 94.9(3), Cl1B–Re1B–N1B 83.9(2), Cl1B–Re1B–N2B 83.33(19), C3B–Re1B–C2B 88.5(3), C3B–Re1B–N1B 96.6(3), C3B–Re1B–N2B 93.5(3), C2B–Re1B–N1B 94.6(3), C2B–Re1B–N2B 169.3(3), N1B–Re1B–N2B 74.7(3).

surface, the H···O/O···H interactions (Fig. 5c) highlight the importance of hydrogen bonds, including CO molecules, in controlling stability together with other physical attributes. It is estimated that the H···Cl/Cl···H interactions contribute 12.5% to the stabilization of the crystal structure of **2**.

2.4. Density functional theory calculations

The bidentate nature of the quinoxaline ligand towards the Re(I) ion and the arrangement of the three CO molecules in a *facial* mode were clearly proved by X-ray crystallographic analysis as well as spectroscopic methods. The local minimum structure of the free ligand **1** was obtained by optimizing the model representing its molecular structure using the Becke 3-parameter (exchange) Lee–Yang–Parr functional[36,37] and the 6-311+G(2d,p) basis set. The crystal data of **1** provided the initial coordinates for the entire optimization process. The validation of the optimized structure as the local minimum structure was performed by executing the vibrational analysis (Fig. S10) at the same level of theory. Similarly, the local minimum structure of Re(I) complex **2** was obtained using the B3LYP/LANL2DZ basis set.[38,39] The atomic coordinates representing the local minimum structures (Fig. S11) of **1** and **2** are tabulated in Tables S3 and S4, respectively. In comparison to the crystal data, selected calculated bond lengths and angles of the local minimum structures of **2** and **3** are given in Table S2. The orientation of the pyridine ring in **1** is theoretically opposite to the experimentally observed orientation. To put it another way, the N1 and N2 atoms (see Fig. 1) are in *trans*-positions experimentally, but theoretically (Fig. S11), they are *cis* to each other. This happens because the calculations are conducted under gaseous conditions, while the X-ray crystallographic analysis deals with molecules that are packed together and interact with one another in the solid state. As experimentally observed, the pyridine ring is not coplanar and rotated from the equatorial plane by 36.6° for the N1–C1–C2–C3 dihedral angle (see Fig. 2). Within |0.002–0.006| Å, the majority of the optimized bond lengths of **1** determined using B3LYP/6-311+G(2d,p) coincide with the crystal data. In particular, the root mean square error in the bond lengths is found to be 0.004 Å. The theoretical and experimental bond lengths fit each other ($d_{\text{calcd.}} = 1.0467 d_{\text{exp}} - 0.0647$) very well linearly, with a regression coefficient approaching one ($R^2 = 0.998$). On the other hand, there is a small difference with a root mean square error of roughly 0.03 Å between the calculated bond lengths and their crystal data of

Open Access Article. Published on 09 January 2026. Downloaded on 6/12/2026 11:25:46 AM.
This article is licensed under a Creative Commons Attribution-NonCommercial 3.0 Unported Licence.

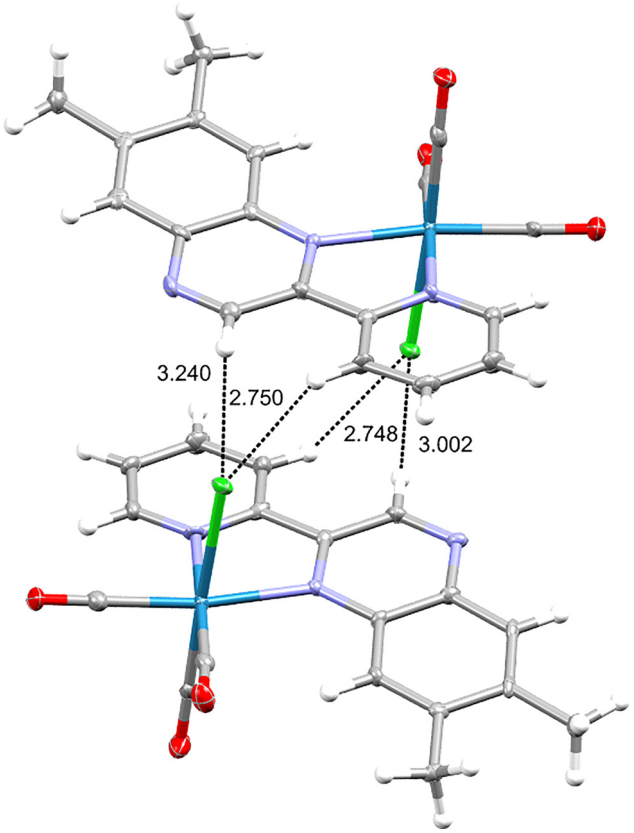

Fig. 3 Selected blue-shifting hydrogen bond interactions in **2**.

the asymmetric unit of **2**. A linear fit ($d_{calcd.}$ = 0.971d_{exp} + 0.0686) was established between the crystal and computed data with R^2 = 0.9977.

Through the natural bond orbital (NBO) analysis of Weinhold and colleagues,[40] utilizing the B3LYP/LANL2DZ level of theory, it was possible to identify the natural charge of the rhenium(I) ion, nature of bonding as well as the hybridization of Re–C, Re–N and Re–Cl bonds in **2**. The electronic arrangement of the Re ion in **2** is [Xe]6s$^{0.41}$5d$^{6.65}$6p$^{0.87}$6d$^{0.02}$7p$^{0.01}$. The total 75.92 electrons in the coordinated metal center are made up of 67.96 core electrons, 7.93 valence electrons, and 0.03 Rydberg electrons. The estimated natural charge on the Re atom is much lower than the formal charge (+1) because of the electron density donation from the five neighbouring ligands. The computed natural charge of Re is −0.921*e*, which may be attributed to the ligand-to-*d*(Re) electron transfer. The *σ*(Re–Cl) bond is formed from an sp$^{3.54}$ (77.97% p) hybrid on the Cl atom and an sp$^{5.80}$d$^{3.87}$ on the Re atom (a mixture of 9.37% s, 54.34% p and 36.29% d). The two *cis* *σ*(Re–C) bonds are created from an sp$^{0.50}$ (33.54% p) hybrid on the C atom and an sp$^{0.70}$d$^{2.13}$ hybrid on the Re atom (a mixture of 26.08% s, 18.34% p and 55.58% d). On the other hand, the axial *cis* *σ*(Re–C) bond is formed from an sp$^{0.52}$ (34.16% p) hybrid on the C atom and an sp$^{3.05}$d$^{2.91}$ hybrid on the Re atom (a mixture of 14.37% s, 43.84% p and 41.78% d). In comparison with the others, the axial *σ*(Re–C) bond is marginally (1–2%) more polarized towards the carbon atom, with about 64.91% of the electron density on the carbon atom. Nonetheless, the axial *σ*(Re–C) bond has 10% less polarization than *σ*(Re–N) (N: pyridine ring). The latter *σ*(Re–N) bond is created from an sp$^{99.97}$(99.76% p) hybrid on the N atom and an sp$^{3.65}$d$^{2.72}$ hybrid on the Re atom (a mixture of 0.38% s, 1.24% p and 98.38% d).

The molecular electrostatic potential (MEP) map, which is associated with electron density, is a very useful tool for characterizing the H-bonding contacts, the sites for electrophilic attack, and nucleophilic reactions. This is related to the dipole moments, partial charges, electronegativity, and chemical reactivity of the molecules. These maps allow us to see portions of a molecule that are noticeably charged. One can determine the interactions between molecules by comprehending the distribution of charges. Different colours show different electrostatic potential values: red indicates areas of the largest negative potential, blue indicates areas of the highest positive potential, and green indicates zero potential. Red, orange, yellow, green, and blue are the possible increments. This MEP computation employed the same methodology used for geometry optimization of **1** and **2**. As shown in Fig. 6, a large negative potential zone in **1** is dispersed throughout the spatial region preferred for the metal ion's coordination, whereas the entire molecule is green (neutral). A small negative potential is on the uncoordinated nitrogen atom of the quinoxaline ligand. On the other hand, the MEP map of **2** (Fig. 6) is distinguished by a strong negative potential on the chlorido ligand and a moderate negative potential on the oxygen atoms of the *facial* CO ligands. The electronegative atoms that were previously indicated are ideal targets for electrophilic attacks or for engaging in intermolecular interactions with biomolecules. A green hue covers the remainder of the MEP map of **2**, except for the pyridine ring's protons and methyl groups.

2.5. Electronic structure

The electronic absorption spectrum of **1**, in acetonitrile (Fig. S12), is characterized by three main transitions at around 210, 258, and 340 nm. The two highest energy transitions may be attributed to the medium- and low-energy π–π* transitions within the benzene ring of the quinoxaline moiety.[41] The lowest energy transition at 340 nm may be assigned to the π–π* transition within the heterocyclic rings. To gain an insight into the nature of the observed absorption bands, the electronic spectrum of **1** was recorded in solvents of different polarity and H-bond tendency [DMSO, DMF, acetonitrile (H-bond donor), methyl alcohol (amphoteric H-bond acceptor–donor), tetrahydrofuran, chloroform, and dichloromethane]. As shown in Fig. 7, changing the nature of the solvent did not alter the wavelength of the lowest energy transition at around 340 nm, indicating that the transition is primarily π–π* with no input from n–π* or charge transfer.

Time-dependent density functional (TDDFT) computations were carried out to shed more light on the nature of the observed electronic transitions. The computations were executed using two levels of theory: B3LYP[36,37]/6-311+G(2d,p) and a Coulomb-attenuated hybrid exchange–correlation functional, CAM-B3LYP[42]/6-311+G(2d,p). The polarizable continuum

 This journal is © The Royal Society of Chemistry and the Centre National de la Recherche Scientifique 2026

Open Access Article. Published on 09 January 2026. Downloaded on 6/12/2026 11:25:46 AM.
This article is licensed under a Creative Commons Attribution-NonCommercial 3.0 Unported Licence.

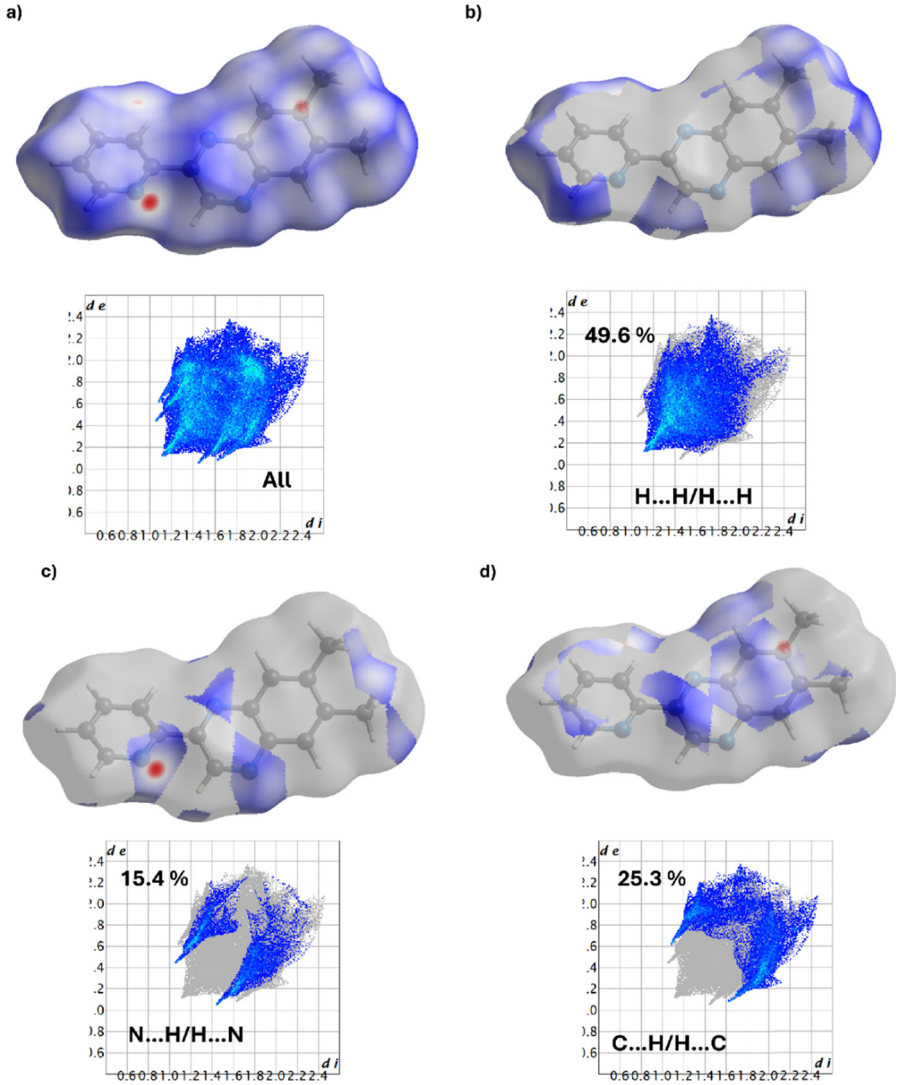

Fig. 4 The full two-dimensional fingerprint plots and their relative Hirshfeld surface for the most abundant interactions in **1**, demonstrating (a) all interactions, and delineated into (b) H···H/H···H, (c) N···H/H···N, and (d) C···H/H···C interactions.

model (PCM)[43] was applied to consider the solvent influence in the calculations. The lowest 30 spin-allowed excitation states were taken into consideration in order to compute the electronic absorption spectra of **1**. To model the computed electronic spectra, Gauss-Sum was employed. With a full width at half maximum of 3000 cm^{-1}, a Gaussian convolution was employed in each excited state. Consideration was given to the calculated excitation state energies with transition strength ($f > 0.1$) (Table S5). The computed electronic absorption spectra of **1** are shown in Fig. S13. The B3LYP spectrum of **1** is characterized by three main bands at 201, 267, and 328 nm in addition to two transitions at 242 and 318 nm. With a difference of just 10 nm, the B3LYP spectrum and the observed one have a good correlation. As shown in Fig. 8, the main electronic transitions at 201, 267 and 328 nm correspond to HOMO−1 → LUMO+3/HOMO−1 → LUMO+4, HOMO−4 → LUMO/HOMO → LUMO+1 and HOMO → LUMO, respectively. It is clear that the HOMO–LUMO transition at 328 nm is mainly π–π* with the whole molecule. On the other hand, the CAM-B3LYP spectrum is characterized by five main bands at 177, 197, 221, 246 and 300 nm. In Fig. 8, the electronic transitions are assigned, and the frontier molecular orbitals responsible for these transitions are described. When compared to the experimental spectrum, it appears that the B3LYP functional predicts the electronic transitions in the UV region more accurately than the other computational methods.

The electronic absorption spectrum of **2**, in dichloromethane (Fig. S14), is characterized by five main transitions at around 228, 256, 280, 362, and 380 nm. There is no discernible change in the wavelengths of the primary electronic transitions when the solvent's polarity and hydrogen bonding tendency are altered, except for the solvent cutoff, which causes some of the bands in the ultraviolet region to vanish (Fig. S15). This suggests that the transitions observed in the electronic absorption spectra of **2** are primarily π–π*. By using TDDFT computations, at the B3LYP/LANL2DZ and CAM-B3LYP/LANL2DZ levels of theory, the

Open Access Article. Published on 09 January 2026. Downloaded on 6/12/2026 11:25:46 AM.
This article is licensed under a Creative Commons Attribution-NonCommercial 3.0 Unported Licence.

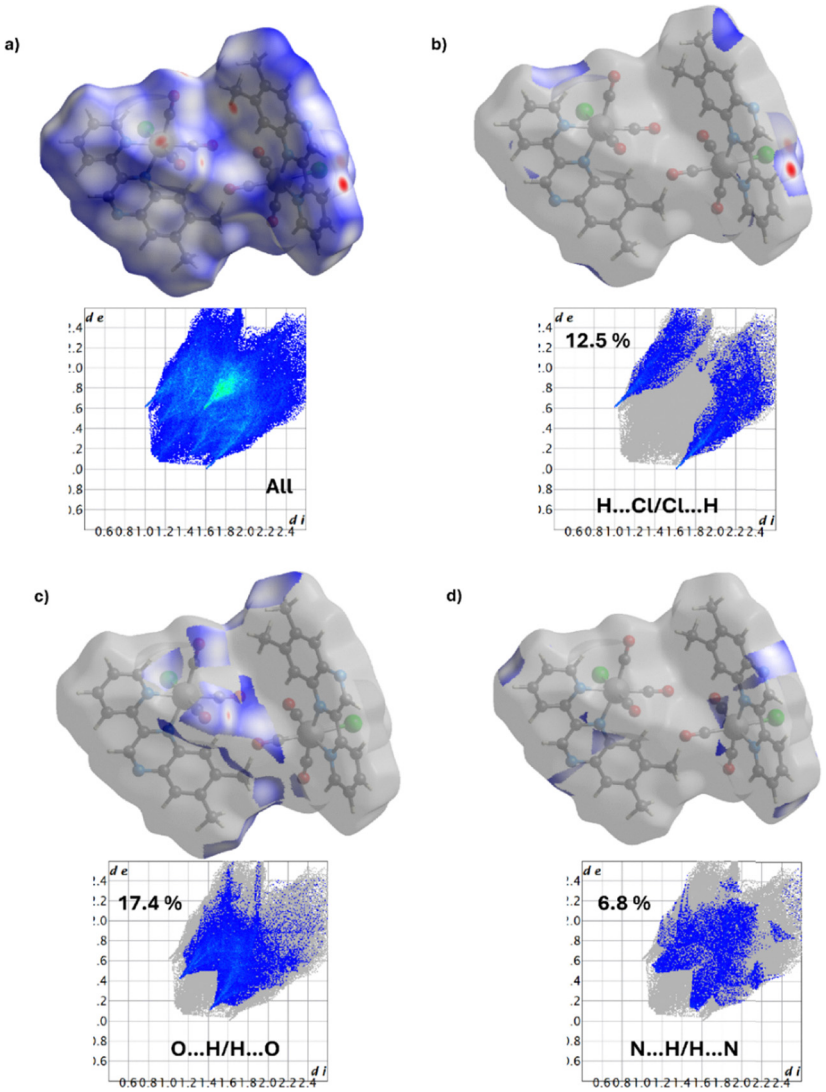

Fig. 5 The full two-dimensional fingerprint plots and their relative Hirshfeld surface for the most abundant interactions in **2**, demonstrating (a) all interactions, and delineated into (b) H···Cl/Cl···H, (c) O···H/H···O, and (d) N···H/H···N interactions.

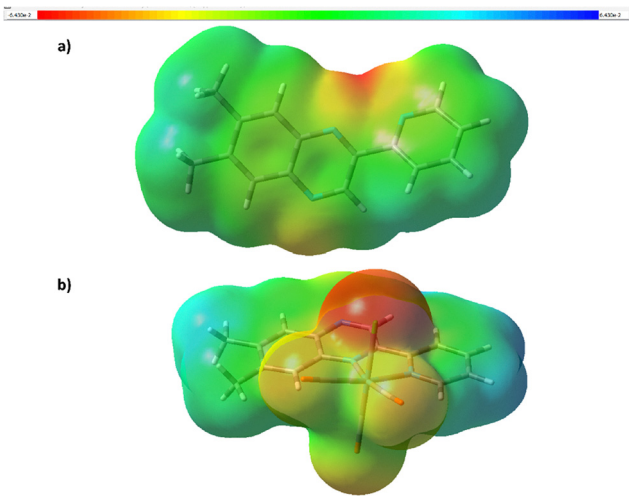

Fig. 6 Molecular electrostatic potential maps of (a) **1** and (b) **2**. The electron density iso-surface is 0.004 a.u.

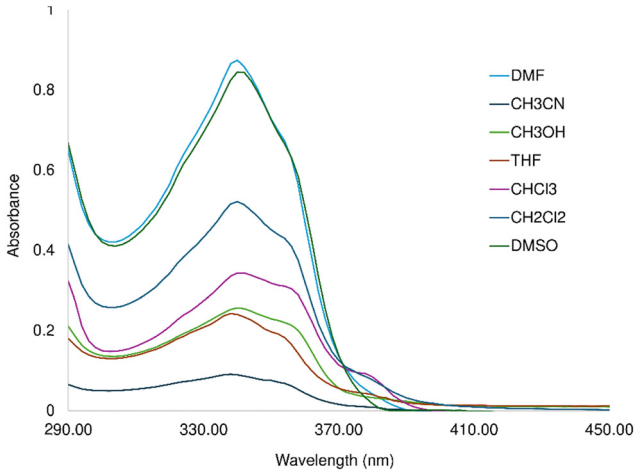

Fig. 7 Electronic absorption spectra of **1** in solvents of different polarities and hydrogen bond tendency.

 This journal is © The Royal Society of Chemistry and the Centre National de la Recherche Scientifique 2026

Open Access Article. Published on 09 January 2026. Downloaded on 6/12/2026 11:25:46 AM.
This article is licensed under a Creative Commons Attribution-NonCommercial 3.0 Unported Licence.

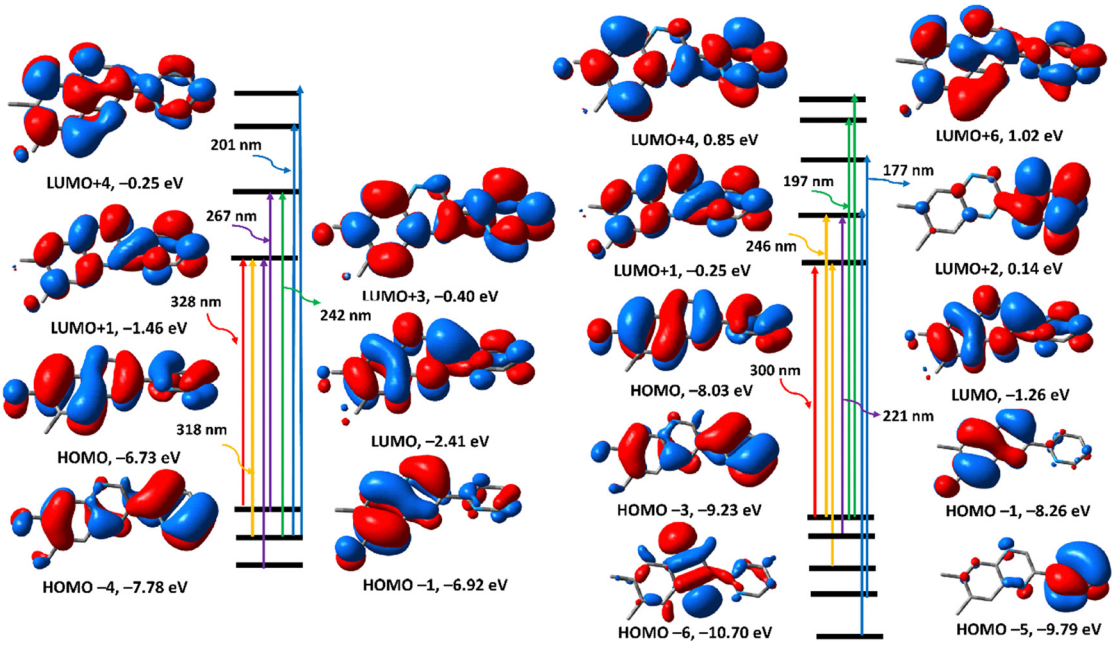

Fig. 8 The calculated selected electronic absorptions of **1** and frontier molecular orbitals responsible for these transitions calculated at the B3LYP/6-311+G(2d,p) (left) and CAM-B3LYP/6-311+G(2d,p) (right) levels.

nature of the electronic transitions observed in **2** has been examined. Fig. S16 displays the calculated electronic absorption spectra of **2**. The B3LYP spectrum of **2** is characterized by three main bands at 276, 360 and 469 nm as well as two shoulders at 255 and 319 nm. The assignments of the calculated spectrum of **2** are shown in Fig. 9. For example, the electronic transition at 360 nm corresponds to HOMO−4 → LUMO. Since the ligand π-framework makes up the majority of both HOMO−4 and LUMO orbitals, the transition at 360 nm may be π–π* in nature. Likewise, the HOMO−1 → LUMO transition at 469 nm is MLCT (metal-to-ligand charge transfer) since it starts at *d*(Re) and ends at the ligand π*-framework. On the other hand, the CAM-B3LYP spectrum of **2** is characterized by four main transitions at 231, 254, 331 and 381 nm corresponding to HOMO−8 → LUMO, HOMO−3 → LUMO+1, HOMO−3 → LUMO and HOMO−1 → LUMO, respectively. Notably, the CAM-B3LYP spectrum of **2** closely

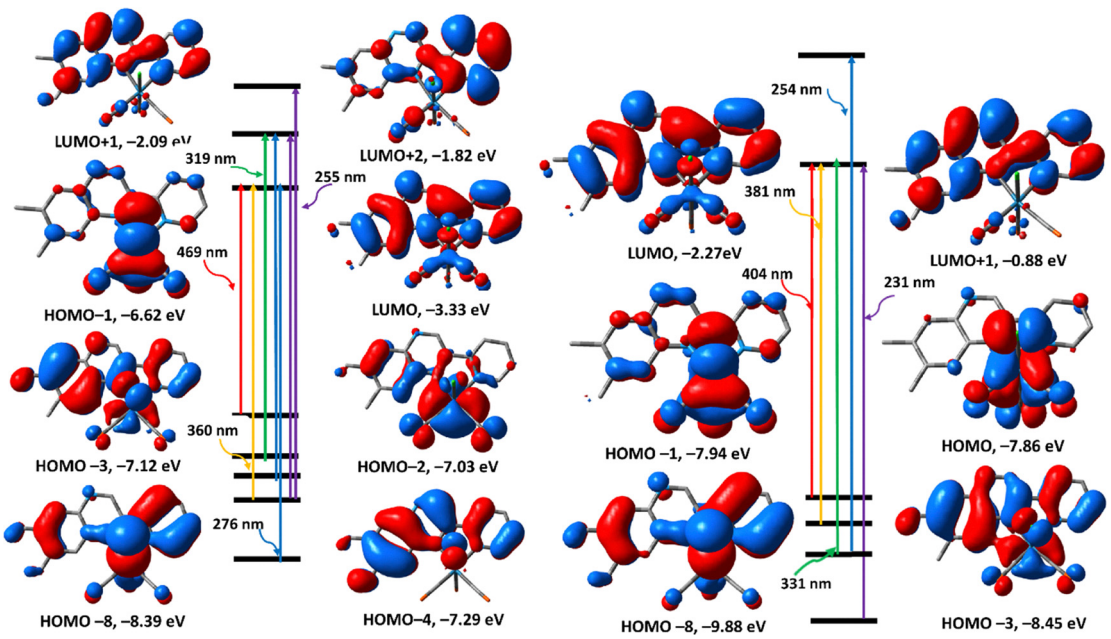

Fig. 9 The calculated selected electronic absorptions of **2** and frontier molecular orbitals responsible for these transitions calculated at the B3LYP/LANL2DZ (left) and CAM-B3LYP/LANL2DZ (right) levels.

Open Access Article. Published on 09 January 2026. Downloaded on 6/12/2026 11:25:46 AM. This article is licensed under a Creative Commons Attribution-NonCommercial 3.0 Unported Licence.

Table 1 MIC values (μg mL^{-1}) of **1** and **2**, as well as the positive controls, determined by the broth microdilution method against selected bacterial and fungal strains

	Minimum inhibitory concentrations (μg mL^{-1})					
	Gram-positive bacteria		Gram-negative bacteria		Fungi	
Compounds	*S. aureus*	*S. pyogenes*	*E. coli*	*P. aeruginosa*	*C. albicans*	*C. tropicalis*
1	600	300	600	4750	600	600
2	410	100	410	810	410	200
Ciprofloxacin	10	10	10	10	—	—
Voriconazole	—	—	—	—	100	100

matches the experimental one. CAM-B3LYP has been shown to accurately predict molecular charge transfer spectra using a long-range correction term.[44,45] Fig. 9 shows the descriptions of the frontier molecular orbitals that took part in the primary transition bands of the CAM-B3LYP computed spectrum. In the later transitions, the HOMOs have major contributions from *d*(Re), whereas the ligand π*-framework forms the LUMO and LUMO+1. Thus, the latter transitions are either ligand-to-ligand charge transfer (LLCT) or MLCT.

2.6. Antimicrobial properties

Coordination and organometallic compounds have so far produced an incredibly high success rate (9.9%) for certain classes of Mn, Co, Zn, Ru, Ag, Ir, Re, Pd, and Pt complexes in screening attempts for possible antibacterial agents compared to organic compounds (0.87%) submitted to the same assays.[4–7,26,46,47] This prompted us to assess the antimicrobial properties of the ligand (**1**) and the rhenium complex (**2**) against six different microorganisms, including two Gram-positive bacteria (*Staphylococcus aureus* and *Streptococcus pyogenes*), two Gram-negative bacteria (*Pseudomonas aeruginosa* and *Escherichia coli*), and two fungal strains (*Candida albicans* and *Candida tropicalis*) in comparison to the reference drugs. Ciprofloxacin was used as a positive control in antibacterial experiments, while voriconazole was used in antifungal studies. The minimum inhibitory concentration (MIC) was ascertained using the broth microdilution dose–response experiment; the results are shown in Table 1. Both compounds performed poorly against the controls. However, the activity exhibited was noteworthy. **2** was superior in activity to **1** with an MIC of 410 μg mL^{-1} and lower for all the microorganisms except *P. aeruginosa*, whereas **1** had 600 μg mL^{-1} as the lowest MIC. *P. aeruginosa* was the most resistant, with **1** exhibiting an MIC of >4000 μg mL^{-1}. Remarkably, **2** still showed relatively good activity with an MIC of 810 μg mL^{-1}. Compound **2** showed the highest potency against *S. pyogenes*.

3. Conclusion

In summary, a novel rhenium(I) tricarbonyl complex bearing the 6,7-dimethyl-2-(pyridin-2-yl)quinoxaline ligand was successfully synthesized and comprehensively characterized. Single-crystal X-ray diffraction confirmed an octahedral geometry with facially coordinated CO ligands and a chelating *N*,*N*′-quinoxaline donor. Weak C–H···Cl interactions were shown by the solid-state crystal structure data to stabilize the crystal packing. DFT and TDDFT studies corroborated the experimental findings and elucidated the nature of Re–L bonding and the electronic transitions responsible for the observed absorption features. The combination of spectroscopic, crystallographic, and theoretical data provides a detailed understanding of the structure–property relationships in this complex, which may inform the design of new rhenium-based compounds for photochemical or bioinorganic applications. While the antimicrobial activity was not high compared to controls, it was noteworthy as a basis for further work.

4. Experimental

4.1. Materials and instruments

All of the organic solvents and reagents used were of analytical grade and were acquired from Sigma-Aldrich in South Africa and Strem Chemicals in Newburyport, USA, unless otherwise noted. The organic solvents and reagents used in these studies were used exactly as supplied, without any additional purification or modification, including *fac*-[ReBr(CO)$_5$], which was used to synthesize the starting material *fac*-[NEt$_4$]$_2$[ReBr$_3$(CO)$_3$].[48] 6,7-Dimethyl-2-(pyridin-2-yl)-quinoxaline **1** was prepared following the published method.[31] Room temperature FT-IR spectra of **1** and **2** were recorded on a PerkinElmer FT-IR spectrometer, operating in the 4000–370 cm^{-1} region. The electronic absorption spectra of the two compounds were recorded on a Thermo Scientific GENESYS 150 UV-visible spectrophotometer. Room temperature NMR spectra (^{1}H and ^{13}C) of **1** and **2** were recorded on a Bruker AXS 400 MHz nuclear magnetic resonance spectrometer operating at 400.00 MHz for ^{1}H and 101.00 MHz for ^{13}C in deuterated solvents such as $CDCl_3$ and acetone-d_6.

4.2. Synthesis

4.2.1. Synthesis of 1. A mixture of 2-acetylpyridine (1.81 g, 15 mmol) and 4,5-dimethylbenzene-1,2-diamine (2.04 g, 15 mmol) was dissolved in methanol (20 mL) in a 100 mL round-bottom flask. A catalytic amount of (SiO_2, ~0.05 g) and aqueous HCl (10%, 2 mL) were added sequentially, and the reaction mixture was refluxed at 85 °C for 24 h under an argon atmosphere. After completion, the mixture was cooled to room temperature, diluted with water, and neutralized with aqueous Na_2CO_3 (10%, 50 mL). The aqueous phase was extracted with chloroform (3 × 100 mL), and the combined organic extracts were washed with water, dried over anhydrous Na_2SO_4, and

 This journal is © The Royal Society of Chemistry and the Centre National de la Recherche Scientifique 2026

Open Access Article. Published on 09 January 2026. Downloaded on 6/12/2026 11:25:46 AM. This article is licensed under a Creative Commons Attribution-NonCommercial 3.0 Unported Licence.

concentrated under reduced pressure. The crude residue was refined by column chromatography on silica gel, eluting with ethyl acetate/*n*-hexane (1 : 1), to afford the pure title compound as an orange solid. Yield: 2.29 g (65%). IR (FT-IR): ν = 2984 (w, CH), 2943 (w, CH), 1589, 1481, 1443, 1210, 1063, 957, 877, 754, 622, 457 cm^{-1}. ^1H NMR (400 MHz, acetone-d_6): δ_H = 9.84 (s, 1H, quinoxaline-H3), 8.77 (d, 1H, $^3J_{H,H}$ = 4.8 Hz, pyridine-H6), 8.59 (d, 1H, $^3J_{H,H}$ = 8.0 Hz, pyridine-H3), 8.02 (td, 1H, $^3J_{H,H}$ = 7.6 Hz, $^4J_{H,H}$ = 1.6 Hz, pyridine-H4), 7.89 (s, 2H, quinoxaline–H5/H8), 7.52 (m, 1H, pyridine-H5), 2.54 (s, 6H, CH_3) ppm. ^{13}C NMR (101 MHz, acetone-d_6): δ_C = 155.5, 150.2, 150.1, 143.7, 142.5, 141.7, 141.3, 138.0, 129.3, 129.1, 125.4, 122.1, 20.2, and 20.1 ppm. UV/vis(methanol): λ_{max} = 340 nm, ε = 2565 M^{-1} cm^{-1}. HR-MS (*m*/*z*): 236.1188 ($[M + H]^+$, calcd), 236.1204 ($[M + H]^+$, found).

4.2.2. Synthesis of 2. Initially, an acidified aqueous solution (5 mL, pH = 2.2; HCl_{aq}) of *fac*-$[NEt_4]_2[Re(CO)_3(Br)_3]$ (0.649 mmol; 500 mg) was treated with three equivalents of silver nitrate solution (1.95 mmol; 331 mg) and then the reaction mixture was allowed to stir for 24 hours at room temperature, forming the aqueous *fac*-$[Re(CO)_3(OH_2)_3]^+$ intermediate. During the 24 hours of stirring, the bromido ligands were exchanged for the chlorido ones, resulting in the formation of *cis*-$[ReCl(CO)_3(OH_2)_2]$. Next, 6,7-dimethyl-2-pyridin-2-yl-quinoxaline (0.649 mmol; 153 mg) dissolved in a minimal amount of acetone was added to the reaction mixture, and stirring was continued for an extra 24 h. Red crystals of the complex were obtained upon crystallization from an acetone/water mixture (25 : 75 v/v). Yield: 76.52% (383 mg; 0.71 mmol). IR (FT IR): ν = 2889 (*w*, CH), 2016 (*vs*, CO), 1881 (*vs*, CO), 1602, 1478, 1338, 1275, 1168, 999, 799, 682, 519 cm^{-1}. ^1H NMR (400 MHz, $CDCl_3$): δ_H = 9.58 (s, 1H, quinoxaline–H3), 9.23 (d, 1H, $^3J_{H,H}$ = 6.8 Hz, pyridine–H6), 8.67 (s, 1H, quinoxaline–H8), 8.48 (d, 1H, $^3J_{H,H}$ = 8.0 Hz, pyridine–H3), 8.16 (td, 1H, $^3J_{H,H}$ = 6.8 Hz, $^4J_{H,H}$ = 1.2 Hz, pyridine–H4), 8.01 (s, 1H, quinoxaline–H5), 7.63 (td, 1H, $^3J_{H,H}$ = 6.0 Hz, $^4J_{H,H}$ = 0.8 Hz, pyridine–H5), 2.65 (s, 3H, CH_3) and 2.59 (s, 3H, CH_3) ppm. ^{13}C NMR (101 MHz, $CDCl_3$): δ_C = 197.0 (CO), 196.3 (CO), 188.2 (CO), 155.9, 153.5, 149.5, 145.4, 144.6, 143.1, 141.7, 139.8, 139.1, 129.5, 127.3, 124.8, 21.0, 20.3 ppm. UV/vis (methanol): λ_{max} = 378 nm, ε = 21 044 M^{-1} cm^{-1}. HR-MS (*m*/*z*): 547.0780 ($[M + CH_3CN–Cl]^+$, calcd.), 547.0779 ($[M + CH_3CN–Cl]^+$, found).

4.3. Single crystal X-ray diffraction analysis

The dichloromethane and acetone/water solutions of **1** and **2**, respectively, gradually evaporated over the course of two weeks, producing crystals suitable for single-crystal X-ray diffraction. Compound **1** was analyzed on a Rigaku XtaLAB Synergy R diffractometer, with a rotating-anode X-ray source and a HyPix CCD detector. Data reduction and absorption were carried out using the CrysAlisPro (version 1.171.40.23a) software package.[49] The X-ray diffraction data for **2** were collected on a Bruker Venture D8 Kappa Photon III C28 equipped with a graphite monochromator using a Mo-Kα X-ray generator operating at a wavelength of 0.71073 Å. Unit cell determination, data integration, and absorption corrections were performed using the Bruker APEX3 software package. The X-ray diffraction measurements were performed at 150.0(10) K for **1** and 100.00(2) for **2** using an Oxford Cryogenics cryostat. The intrinsic phasing approach (SHELXT program) was exploited to solve the framework of the metal complex,[50] which was then enhanced using the SHELXL program and the SHELXLE graphical user interface.[51] Non-hydrogen atoms were refined by anisotropic approximation, while hydrogen atoms were 'riding' on idealised sites. The notable negative residual electron density in **2** is located in regions of weak diffuse solvent/background scattering and does not correspond to chemically meaningful positions. These residual features are therefore attributed to termination effects and minor Fourier truncation associated with the weakly scattering lattice water.

4.4. Density functional theory calculations

The crystal data of **1** and **2** provided the initial coordinates for the entire optimization process. The ground state geometry optimization of **1** and **2**, as well as their vibrational analysis, were conducted using the B3LYP functional[37,52] and the 6-311+G(2d,p) basis set (LANL2DZ basis set in the case of **2**).[38,39] The literature frequently reports a similar methodology for DFT calculations of compounds based on the same metal ion.[53,54] The acquired optimised structures were confirmed to be local minima, as they exhibit the lowest energy on the potential energy surface, based on the vibrational modes (no imaginary frequencies). The atomic coordinates of the lowest energy ground-state optimized structures of **1** and **2** are tabulated in Tables S3 and S4. The calculated vibrational spectra of **1** and **2** are shown in Fig. S9. For the two compounds, TDDFT calculations were performed using the B3LYP and CAM-B3LYP functionals[42]; for compound **1**, the basis set was 6-311+G(2d,p); and for complex **2**, the basis set was LANL2DZ. All the computations were carried out using Gaussian03 software.[55] The electronic and vibrational spectra, as well as frontier molecular orbitals, were visualized using GaussView03.[56]

4.5. Antimicrobial assays

The microorganisms used in this investigation were sourced from the culture collections maintained at the Microbiology Laboratory within the Department of Pharmaceutical Sciences at Tshwane University of Technology, Arcadia Campus, South Africa. The bacterial panel comprised both Gram-positive strains, *Staphylococcus aureus* and *Streptococcus pyogenes*, and Gram-negative strains, *Escherichia coli* and *Pseudomonas aeruginosa*. The fungal strains (*Candida albicans* and *Candida tropicalis*) were included for antifungal evaluation. Bacterial and fungal pre-cultures were propagated in tryptic soy broth (TSB) and Sabouraud dextrose broth (SDB), respectively, to ensure active growth before testing. The minimum inhibitory concentrations (MICs) of **1** and **2** were determined using the serial microdilution technique, as outlined in the protocol by ref. 57. In this protocol, under sterile conditions, 96-well microtiter plates were prepared by dispensing 100 μL of sterile distilled water into each well. The samples were diluted in acetone and then 100 μL of the samples were transferred to the first rows. A serial doubling dilution was performed, followed

Open Access Article. Published on 09 January 2026. Downloaded on 6/12/2026 11:25:46 AM. This article is licensed under a Creative Commons Attribution-NonCommercial 3.0 Unported Licence.

by the addition of 100 μL of the microbial suspension (1×10^8) to each well. The ideal conditions for incubation (37 °C for 24 h for bacteria and 48 h for the fungi) were followed. In all repetitions of the MIC to validate the sensitivity of the microbial cultures, commercial antimicrobials (ciprofloxacin for bacteria and voriconazole for fungi) were included in the dosing with initial concentrations of 0.01 mg mL^{-1} and 0.10 mg mL^{-1}, respectively, to validate the sensitivity of the microbial cultures. A negative was included for the dilution (acetone) to ensure that the diluent did not affect the antimicrobial action. A 0.4 mg mL^{-1} *p*-iodonitrotetrazolium violet (INT) solution was prepared and 40 μL was transferred into all the wells within which the suspension had been inoculated. The microtiter plates with bacteria were examined after 6 h to see if there was any colour change in relation to the concentration of microbial growth, whereas those containing fungi were checked after 24 h. The assays were performed in triplicate to ensure the data were consistent and reproducible.

Author contributions

Sibusiso A. Sithole: writing – original draft, visualization, methodology, investigation, formal analysis, data curation, conceptualization. Ahmed M. Mansour: writing – original draft, visualization, methodology, investigation, formal analysis, data curation, conceptualization. Frederick P. Malan: writing – review & editing, methodology, data curation. Gurusamy Manikandan: writing – review & editing, methodology, data curation. David R. Katerere: writing – review & editing, supervision. Ola R. Shehab: writing – original draft, visualization, methodology, investigation, formal analysis, data curation, conceptualization. Amanda-Lee E. Manicum: writing – review & editing, supervision, methodology, data curation, conceptualization.

Conflicts of interest

The authors declare that they have no known competing financial interests or personal relationships that could have appeared to influence the work reported in this paper.

Data availability

The data supporting this article have been included as part of the supplementary information (SI). Supplementary information is available. See DOI: https://doi.org/10.1039/d5nj04125b.

All data are available from the authors upon request.

CCDC 2433822 (**1**) and 2433551 (**2**) contain the supplementary crystallographic data for this paper.[58a,b]

Acknowledgements

This work is based on the research financially supported by the National Research Foundation of South Africa under the Thuthuka program (Grant No. 113629). We want to extend our gratitude to the Tshwane University of Technology, the Department of Chemistry (Inorganic Chemistry Group), and the Department of Pharmaceutical Science (PB2A Research Group) for the support. The authors acknowledge that the opinions, findings, conclusions, or recommendations expressed in this publication do not necessarily reflect the views of the National Research Foundation of South Africa.

References

1 K. K.-W. Lo, W.-K. Hui, C.-K. Chung, K. H.-K. Tsang, D. C.-M. Ng and N. Zhu, *et al.*, Biological labelling reagents and probes derived from luminescent transition metal polypyridine complexes, *Coord. Chem. Rev.*, 2005, **249**(13–14), 1434–1450.

2 T. Yu, D. P. K. Tsang, V. K. M. Au, W. H. Lam, M. Y. Chan and V. W. W. Yam, Deep Red to Near-Infrared Emitting Rhenium(I) Complexes: Synthesis, Characterization, Electrochemistry, Photophysics, and Electroluminescence Studies, *Chem. – Eur. J.*, 2013, **19**(40), 13418–13427.

3 C. Sun, S. Prosperini, P. Quagliotto, G. Viscardi, S. S. Yoon and R. Gobetto, *et al.*, Electrocatalytic reduction of CO 2 by thiophene-substituted rhenium(I) complexes and by their polymerized films, *Dalton Trans.*, 2016, **45**(37), 14678–14688.

4 K. Schindler, Y. Cortat, M. Nedyalkova, A. Crochet, M. Lattuada and A. Pavic, *et al.*, Antimicrobial activity of rhenium di-and Tricarbonyl diimine complexes: insights on membrane-Bound S. aureus protein binding, *Pharmaceuticals*, 2022, **15**(9), 1107.

5 E. K. Towett, V. J. Tembu, D. Kemboi, M. K. Langat and A.-L. E. Manicum, Review of Recent Medicinal Applications of Rhenium(I) Tricarbonyl Complexes, *Int. J. Mol. Sci.*, 2025, **26**(14), 7005.

6 K. Schindler and F. Zobi, Anticancer and antibiotic rhenium tri-and dicarbonyl complexes: current research and future perspectives, *Molecules*, 2022, **27**(2), 539.

7 A. M. Mansour, Pyridylbenzimidazole based Re(I)(CO) 3 complexes: antimicrobial activity, spectroscopic and density functional theory calculations, *RSC Adv.*, 2019, **9**(26), 15108–15114.

8 A. Domenichini, I. Casari, P. V. Simpson, N. M. Desai, L. Chen and C. Dustin, *et al.*, Rhenium N-heterocyclic carbene complexes block growth of aggressive cancers by inhibiting FGFR-and SRC-mediated signalling, *J. Exp. Clin. Cancer Res.*, 2020, **39**(1), 276.

9 P. Collery, V. Veena, A. Harikrishnan and D. Desmaele, The rhenium(I)-diselenoether anticancer drug targets ROS, TGF-β1, VEGF-A, and IGF-1 in an in vitro experimental model of triple-negative breast cancers, *Invest. New Drugs*, 2019, **37**(5), 973–983.

10 P. Collery, F. Santoni, J. Ciccolini, T. N. N. Tran, A. Mohsen and D. Desmaele, Dose effect of rhenium(I)-diselenoether as anticancer drug in resistant breast tumor-bearing mice after repeated administrations, *Anticancer Res.*, 2016, **36**(11), 6051–6057.

11 A. Kumar, S.-S. Sun and A. J. Lees, Photophysics and photochemistry of organometallic rhenium diimine complexes, in *Photophysics of Organometallics*, 2009, pp. 37–71.

 This journal is © The Royal Society of Chemistry and the Centre National de la Recherche Scientifique 2026

Open Access Article. Published on 09 January 2026. Downloaded on 6/12/2026 11:25:46 AM. This article is licensed under a Creative Commons Attribution-NonCommercial 3.0 Unported Licence.

12 E. E. Langdon-Jones, N. O. Symonds, S. E. Yates, A. J. Hayes, D. Lloyd and R. Williams, *et al.*, Fluorescent rhenium-naphthalimide conjugates as cellular imaging agents, *Inorg. Chem.*, 2014, **53**(7), 3788–3797.

13 M. Sagnou, S. Tzanopoulou, C. P. Raptopoulou, V. Psycharis, H. Braband and R. Alberto, *et al.*, A Phenylbenzothiazole Conjugate with the Tricarbonyl *fac*-[M(I)(CO) 3] + (M = Re, 99Tc, 99mTc) Core for Imaging of β-Amyloid Plaques, *Eur. J. Inorg. Chem.*, 2012, 4279–4286.

14 E. B. Bauer, A. A. Haase, R. M. Reich, D. C. Crans and F. E. Kühn, Organometallic and coordination rhenium compounds and their potential in cancer therapy, *Coord. Chem. Rev.*, 2019, **393**, 79–117.

15 K. Łyczko, A. Pogorzelska, U. Częścik, M. Koronkiewicz, J. E. Rode and E. Bednarek, *et al.*, Tricarbonyl rhenium(i) complexes with 8-hydroxyquinolines: structural, chemical, antibacterial, and anticancer characteristics, *RSC Adv.*, 2024, **14**(25), 18080–18092.

16 M. Wenzel, M. Patra, C. H. R. Senges, I. Ott, J. J. Stepanek and A. Pinto, *et al.*, Analysis of the Mechanism of Action of Potent Antibacterial Hetero-tri-organometallic Compounds: A Structurally New Class of Antibiotics, *ACS Chem. Biol.*, 2013, **8**(7), 1442–1450.

17 S. N. Sovari, S. Vojnovic, S. S. Bogojevic, A. Crochet, A. Pavic and J. Nikodinovic-Runic, *et al.*, Design, synthesis and in vivo evaluation of 3-arylcoumarin derivatives of rhenium(ı) tricarbonyl complexes as potent antibacterial agents against methicillin-resistant Staphylococcus aureus (MRSA), *Eur. J. Med. Chem.*, 2020, **205**, 112533.

18 S. N. Sovari, N. Radakovic, P. Roch, A. Crochet, A. Pavic and F. Zobi, Combatting AMR: A molecular approach to the discovery of potent and non-toxic rhenium complexes active against C. albicans-MRSA co-infection, *Eur. J. Med. Chem.*, 2021, **226**, 113858.

19 K. Schindler, G. Demirci, B. Tran, S. N. Sovari, Y. Cortat and N. F. R. De Sousa, *et al.*, Boosting Antibiotic Efficacy of Azole Drugs against Methicillin-Resistant Staphylococcus Aureus by Coordination to Rhenium Carbonyl Complexes, *ChemBioChem*, 2025, **26**(16), e202500368.

20 M. Patra, M. Wenzel, P. Prochnow, V. Pierroz, G. Gasser and J. E. Bandow, *et al.*, An organometallic structure-activity relationship study reveals the essential role of a Re (CO) 3 moiety in the activity against Gram-positive pathogens including MRSA, *Chem. Sci.*, 2015, **6**(1), 214–224.

21 D. Siegmund, N. Lorenz, Y. Gothe, C. Spies, B. Geissler and P. Prochnow, *et al.*, Benzannulated Re (i)–NHC complexes: Synthesis, photophysical properties and antimicrobial activity, *Dalton Trans.*, 2017, **46**(44), 15269–15279.

22 A. Frei, M. Amado, M. A. Cooper and M. A. Blaskovich, Light-Activated rhenium complexes with dual mode of action against bacteria, *Chem. – Eur. J.*, 2020, **26**(13), 2852–2858.

23 L. C.-C. Lee, K.-K. Leung and K. K.-W. Lo, Recent development of luminescent rhenium(ı) tricarbonyl polypyridine complexes as cellular imaging reagents, anticancer drugs, and antibacterial agents, *Dalton Trans.*, 2017, **46**(47), 16357–16380.

24 S. V. Kumar, W. K. Lo, H. J. Brooks, L. R. Hanton and J. D. Crowley, Antimicrobial properties of mono-and di-*fac*-rhenium tricarbonyl 2-pyridyl-1, 2, 3-triazole complexes, *Aust. J. Chem.*, 2015, **69**(5), 489–498.

25 S. S. Mendes, J. Marques, E. Mesterházy, J. Straetener, M. Arts and T. Pissarro, *et al.*, Synergetic Antimicrobial Activity and Mechanism of Clotrimazole-Linked CO-Releasing Molecules, *ACS Bio & Med Chem Au*, 2022, **2**(4), 419–436.

26 A. Frei, M. Amado, M. A. Cooper and M. A. T. Blaskovich, Light-Activated Rhenium Complexes with Dual Mode of Action against Bacteria, *Chem. – Eur. J.*, 2020, **26**(13), 2852–2858.

27 T. N. Moshkina, E. V. Nosova, A. E. Kopotilova, M. I. Savchuk, I. L. Nikonov and D. S. Kopchuk, *et al.*, Synthesis and photophysical properties of pyridyl-and quinolinyl-substituted 4-(4-aminophenyl) quinazolines, *J. Photochem. Photobiol., A*, 2022, **429**, 113917.

28 P. S. Auti, G. George and A. T. Paul, Recent advances in the pharmacological diversification of quinazoline/quinazolinone hybrids, *RSC Adv.*, 2020, **10**(68), 41353–41392.

29 T. Gupta, A. Rohilla, A. Pathak, M. J. Akhtar, M. R. Haider and M. S. Yar, Current perspectives on quinazolines with potent biological activities: A review, *Synth. Commun.*, 2018, **48**(10), 1099–1127.

30 S. Srivastava and S. Srivastava, Biological activity of Quinazoline: a review, *Int. J. Pharma Sci. Res.*, 2015, **6**(9), 1206–1213.

31 S. Muthuramalingam, T. Khamrang, M. Velusamy and R. Mayilmurugan, Catalytic fixation of atmospheric carbon dioxide by copper (II) complexes of bidentate ligands, *Dalton Trans.*, 2017, **46**(46), 16065–16076.

32 R. M. Khaled, M. T. Abo-Elfadl, K. Radacki, M. A. A. Zeid, O. R. Shehab and N. S. Abdel-Kader, *et al.*, Visible-light-induced CO-releasing properties and cytotoxicity of a Ru (II) carbonyl complex containing 2-(pyridin-2-yl)-quinoxaline, *Dalton Trans.*, 2025, **54**(6), 2529–2539.

33 R. M. Khaled, K. Radacki, G. A. Mostafa, E. A. Ali, O. R. Shehab and A. M. Mansour, Light-mediated CO release from a tricarbonyl manganese (i) complex with a bidentate quinoxaline ligand, *RSC Adv.*, 2025, **15**(35), 28642–28650.

34 P. R. Spackman, M. J. Turner, J. J. McKinnon, S. K. Wolff, D. J. Grimwood and D. Jayatilaka, *et al.*, CrystalExplorer: a program for Hirshfeld surface analysis, visualization and quantitative analysis of molecular crystals, *J. Appl. Crystallogr.*, 2021, **54**(3), 1006–1011.

35 M. A. Spackman and D. Jayatilaka, Hirshfeld surface analysis, *CrystEngComm*, 2009, **11**(1), 19–32.

36 A. Becke, Density-functional thermochemistry. III. The role of exact exchange, *J. Chem. Phys.*, 1993, **98**, 5648.

37 A. D. Becke, Density-functional exchange-energy approximation with correct asymptotic behavior, *Phys. Rev. A: At., Mol., Opt. Phys.*, 1988, **38**(6), 3098.

38 P. J. Hay and W. R. Wadt, Ab initio effective core potentials for molecular calculations. Potentials for K to Au including the outermost core orbitals, *J. Chem. Phys.*, 1985, **82**(1), 299–310.

Open Access Article. Published on 09 January 2026. Downloaded on 6/12/2026 11:25:46 AM. This article is licensed under a Creative Commons Attribution-NonCommercial 3.0 Unported Licence.

39 P. J. Hay and W. R. Wadt, Ab initio effective core potentials for molecular calculations. Potentials for the transition metal atoms Sc to Hg, *J. Chem. Phys.*, 1985, **82**(1), 270–283.
40 A. E. Reed, L. A. Curtiss and F. Weinhold, Intermolecular interactions from a natural bond orbital, donor-acceptor viewpoint, *Chem. Rev.*, 1988, **88**(6), 899–926.
41 O. R. Shehab and A. M. Mansour, Exploring electronic structure, and substituent effect of some biologically active benzimidazole derivatives: Experimental insights and DFT calculations, *J. Mol. Struct.*, 2021, **1223**, 128996.
42 T. Yanai, D. P. Tew and N. C. Handy, A new hybrid exchange–correlation functional using the Coulomb-attenuating method (CAM-B3LYP), *Chem. Phys. Lett.*, 2004, **393**(1–3), 51–57.
43 M. Cossi, V. Barone, R. Cammi and J. Tomasi, Ab initio study of solvated molecules: a new implementation of the polarizable continuum model, *Chem. Phys. Lett.*, 1996, **255**(4), 327–335.
44 D. A. Habashy, R. M. Khaled, A. Y. Ahmed, K. Radacki, S. K. Ahmed and E. K. Tharwat, *et al.*, Cytotoxicity of *fac*-Mn(CO)3 complexes with a bidentate quinoline ligand towards triple negative breast cancer, *Dalton Trans.*, 2022, **51**(37), 14041–14048.
45 A. M. Mansour, R. M. Khaled, K. Radacki, Z. Younes, M. Gamal and B. Guirguis, *et al.*, In vitro cytotoxicity of Mn(i) and Ru(ii) carbonyls with a diphenyl pyridyl phosphine coligand towards leukaemia, *Dalton Trans.*, 2023, **52**(30), 10286–10293.
46 A. Frei, J. Zuegg, A. G. Elliott, M. Baker, S. Braese and C. Brown, *et al.*, Metal complexes as a promising source for new antibiotics, *Chem. Sci.*, 2020, **11**(10), 2627–2639.
47 A. Frei, A. G. Elliott, A. Kan, H. Dinh, S. Bräse and A. E. Bruce, *et al.*, Metal complexes as antifungals? From a crowd-sourced compound library to the first in vivo experiments, *JACS Au*, 2022, **2**(10), 2277–2294.
48 R. A. Alberto, R. Schibli, P. A. Schubiger, U. Abram and T. Kaden, Reactions with the technetium and rhenium carbonyl complexes $(NEt_4)_2[MX_3(CO)_3]$. Synthesis and structure of $[Tc(CN\text{-}But)_3(CO)_3](NO_3)$ and $(NEt_4)[Tc_2(\mu\text{-}SCH_2CH_2OH)_3(CO)_6]$, *Polyhedron*, 1996, **15**, 1079–1089.
49 O. Rigaku, *CrysAlis PRO Soft. Syst*, Rigaku Corporation, Oxford, 2018.
50 G. M. Sheldrick, SHELXT–Integrated space-group and crystal-structure determination, *Acta Crystallogr., Sect. A: Found. Adv.*, 2015, **71**(1), 3–8.
51 G. M. Sheldrick, A short history of SHELX, *Acta Crystallogr., Sect. A: Found. Crystallogr.*, 2008, **64**(1), 112–122.
52 A. D. Becke, Density-functional thermochemistry. III. The role of exact exchange, *J. Chem. Phys.*, 1993, **98**, 5648.
53 M. T. Abo-Elfadl and A. M. Mansour, Cytotoxic properties of *fac*-Re $(CO)_3$ complexes with quinoline coligands: Insights on the mode of cell death and DNA fragmentation, *Inorg. Chim. Acta*, 2023, **553**, 121521.
54 A. M. Mansour, N. M. Ibrahim, A. M. Farag and M. T. Abo-Elfadl, Evaluation of cytotoxic properties of two fluorescent *fac*-$Re(CO)_3$ complexes bearing an *N,N*-bidentate benzimidazole coligand, *RSC Adv.*, 2022, **12**(47), 30829–30837.
55 M. J. Frisch, G. W. Trucks, H. B. Schlegel, G. E. Scuseria, M. A. Robb and J. R. Cheeseman, *et al.*, *Gaussian 03 (Revision A9)*, Gaussian, Inc, Pittsburgh, 2003.
56 A. Frisch, A. B. Nielson and A. J. Holder, *Gaussview User Manual*, Gaussian, Inc, Pittsburgh, PA. 2000.
57 J. N. Eloff, A sensitive and quick microplate method to determine the minimal inhibitory concentration of plant extracts for bacteria, *Planta Med.*, 1998, **64**(8), 711–713.
58 (*a*) CCDC 2433822: Experimental Crystal Structure Determination, 2025, DOI: 10.5517/ccdc.csd.cc2mpldb; (*b*) CCDC 2433551: Experimental Crystal Structure Determination, 2025, DOI: 10.5517/ccdc.csd.cc2mp9n9.

 This journal is © The Royal Society of Chemistry and the Centre National de la Recherche Scientifique 2026